PERGAMON

International Journal of Solids and Structures 37 (2000) 4477–4507

INTERNATIONAL JOURNAL OF SOLIDS and STRUCTURES

www.elsevier.com/locate/ijsolstr

Dynamic deformation and fracture behavior of novel damage tolerant discontinuously reinforced aluminum composites

M.A. Irfan, V. Prakash*

Department of Mechanical and Aerospace Engineering, Case Western Reserve University, 10900 Euclid Avenue, Cleveland OH 44106-7222, USA

Received 11 May 1998

Abstract

Extrinsically toughened discontinuously reinforced aluminum composites are processed with the objective of enhancing damage tolerance of conventional particle reinforced aluminum composites. The approach consists of producing a composite microstructure in which discrete ductile phases have been incorporated into the particle reinforced metal matrix via traditional powder processing routes. The present study focuses on investigating the effects of volume fraction and flow strength of the ductile phase reinforcements in determining dynamic deformation and fracture characteristics of these extrinsically toughened composites. The dynamic compression behavior of the composites is examined by employing the split Hopkinson pressure bar. The measured dynamic stress–strain response of the composites is correlated with the macro- and micro-damage mechanisms inferred from post examination of the impacted specimens. The dynamic fracture characteristics of the composites are obtained by impact loading pre-cracked three point bend specimens in a modified Hopkinson bar apparatus. The measured load-point force versus load-point displacement curves are used to, (a) estimate the energy required for dynamic crack initiation, and (b) understand the interaction of the dynamically propagating crack tip with the ductile phase reinforcements. The results indicate that the extrinsically toughened DRA composites absorb significantly greater energy during the crack propagation as compared to the conventional DRA composites. Also, the level of extrinsic toughening introduced in the composites is affected by the location, volume fraction and mechanical properties of the ductile phase reinforcements. Amongst the relatively larger volume fraction ductile-phase reinforced composites, the ductile phase reinforcements comprising low flow strength commercial purity aluminum fail primarily in a ductile manner, whereas the ductile phase reinforcements comprising high strength Al alloy fail in a cleavage manner by inter-granular fracture.

Keywords: Metal matrix composites; Extrinsic toughening; Layered materials; Split Hopkinson pressure bar; Dynamic compressive behavior; Dynamic fracture; Crack propagation gage

* Corresponding author. Fax: +1-216-368-6445.
E-mail address: vxp18@po.cwru.edu (V. Prakash).

0020-7683/00/$ - see front matter
PII: S0020-7683(99)00195-X

1. Introduction

Metal matrix composites (MMCs), with continuous brittle reinforcements (ceramic fibers) and/or discontinuous brittle reinforcements (ceramic whiskers or particulates), offer the potential for significant improvement in mechanical performance over monolithic metallic alloys in several structural applications. In particular, in recent years interest in discontinuous reinforced composites has increased dramatically over their continuous fiber reinforced counterparts since whisker/particulate reinforcements invariably lead to composites with, (a) a greater degree of isotropy, which is desirable in many structural applications, and (b) are lower in cost to manufacture since they can be formed by conventional manufacturing practices such as forging, rolling and extrusion.

The increasing interest in particulate reinforced MMCs has been driven largely by their mechanical, thermal and wear properties such as high specific stiffness, high specific strength, high thermal conductivity, good oxidation and wear resistance, to name a few. These properties have made these composites a strong candidate for use within the aerospace, automotive, electronic and recreational industries. Despite the positive influences of ceramic particulate reinforcement on the composite properties, the inherent brittle nature of these reinforcements generally decreases the ductility as well as the fracture toughness. For example, the ductility of the ceramic particulate reinforced MMC is observed to be substantially lower (approximately one-fifth) than that of the metal matrix material alone, while the fracture toughness of the MMCs is typically one-fourth of the un-reinforced alloy.

In view of the vast commercial potential of particle reinforced MMCs, significant scientific efforts have been devoted to studying their quasi-static and dynamic mechanical properties. From these studies it is now fairly well understood that the physical properties of these composites, such as the elastic modulus and the Poisson's ratio, are controlled primarily by the volume fraction of the brittle reinforcement phase. However, the relationship between the strength and the reinforcement volume fraction is much more complex. The composite strength is affected by several other material parameters in addition to the volume fraction of reinforcement. For example, the strength of the metal matrix alloy is observed to strongly influence the effect of reinforcement on the composite strength. When a low strength alloy, such as the 6061 Al alloy, is reinforced with 15% silicon carbide particulates (SiC_p), the typical increase in composite strength is about 50%. However, when a high strength matrix alloy is reinforced with SiC_p, the strength of the composite is observed to be the same as the monolithic matrix alloy or may be even less (Manoharan et al., 1993). The premature loss of ductility has been largely attributed to microscopic failure mechanisms that result from the presence of brittle reinforcement phase in a relatively soft matrix. While the hard reinforcement particles can greatly enhance the strength of these composites, they also provide sites for the initiation of damage during plastic deformation. One of the primary damage mechanisms is particle cracking, although failure in the matrix and near the particle–matrix interface have also been observed. The latter modes of damage predominate when the reinforcements are sufficiently strong or when aging precipitates in the matrix provide preferential sites for void nucleation. Moreover, catastrophic failure in such materials appear to occur by the coalescence of the evolving damage, either by impingement of adjacent voids or by strain localization in the ligament between the voids.

In contrast to mechanical behavior under quasi-static loading, the present state of understanding of deformation and failure in particle reinforced MMCs under dynamic loading conditions is still in its infancy. In some initial studies on whisker reinforced MMCs, Harding et al. (1987) reported a very weak strain rate sensitivity of flow stress at room temperature in a SiC_w/2124 Al matrix composite. Marchand et al. (1988) and Cho et al. (1991) reported an increase in dynamic fracture toughness of SiC_w/2124 Al matrix composite when compared with its quasi-static fracture toughness. However, the dynamic fracture toughness was observed to decrease as the volume fraction of the reinforcement was increased. Perng et al. (1993) reported an increase in strain-rate sensitivity of flow stress with increasing

reinforcement content for an Al_2O_3/6061-T6 Al composite at low test temperatures. Hong et al. (1993) conducted an experimental study to investigate dynamic compressive strength of an Al–Zn–Mg–Cu alloy matrix with 20% SiC reinforcement. The strain hardening rates of the over-aged composites and the control alloys were found to be lower than their under-aged counterparts. However, the over-aged composites and the control alloys show higher strain-rate sensitivity as compared to the under-aged composites. Also, in both the over-aged and the under-aged cases, the flow strength of the composites was observed to decrease at plastic strains larger than 0.15. The decrease in strength was attributed to the onset of damage in the form of micro-cracks at the particle–matrix interface. Chichili and Ramesh (1995) studied the dynamic behavior of alumina particle reinforced 6061-T6 Al alloy metal matrix composite using a tension/compression Hopkinson bar. They reported differences in strain hardening rates in dynamic tension and compression. The stress–strain curves in dynamic tension were found to show negligible hardening, whereas the dynamic compression response of the same material showed substantial strain hardening. These differences in strain hardening rates were attributed to material softening due to the accumulation of microstructural damage within the composite when loaded in tension. Yadav et al. (1995) observed that the strengthening of 6061-T6 Al composites reinforced with 20 vol% alumina particles continued into the high strain rate regime, and at elevated strain rates the metal matrix composite displays significantly greater strain rate sensitivity when compared to the monolithic alloy.

In recent years, a number of attempts have been made to improve the fracture toughness of particle reinforced composites utilizing both intrinsic and extrinsic toughening methodologies (Osman et al., 1995). Intrinsic toughening deals primarily with modifications of the grain structure of the matrix, variation in particle size and shape, and particle/matrix interface characteristics. On the other hand, the objective of extrinsic toughening is to segregate the composite into specific particle rich brittle regions interleaved with tough monolithic ductile phase regions. The particle rich regions provide the required enhancement in mechanical properties, whereas the tough ductile phase enhances the toughness of the composites. Composite material development, utilizing the concept of extrinsically toughened composite microstructures, have traditionally focused on laminate structures comprising alternating layers of discontinuously reinforced metal matrix composites (a *semi-brittle* component) and a monolithic metallic alloy (a more *ductile* component). Such ductile/brittle laminates contain discrete interfaces and have generally been produced via press bonding or roll bonding of alternating ductile/brittle laminae. Increased fracture toughness and impact energies, as compared to the discontinuously reinforced aluminum (DRA) composites have been reported in these (Embury et al., 1967; Sherby et al., 1990; Syn et al., 1991). While the laminate approach has provided extrinsic toughening via the introduction of discrete interfaces, Nardone et al. (1991) have utilized other potential cost effective approaches to extrinsic toughening by developing microstructurally toughened structures which involve fewer discrete interfaces separating the ductile/brittle constituents. The notch impact energy of these structures have been an order of magnitude higher as compared to conventional DRA composites with the same volume fraction of the reinforcement.

Continuing the efforts to improve the impact toughness of DRA composites via the extrinsic toughening approach, recently novel extrinsically toughened composites have been developed in which ductile, high toughness particle free regions are compartmentalized and discrete from the brittle particle reinforced regions. These composites are produced by introducing ductile phase reinforcements during the powder blending phase of the manufacturing process and then extruding the composite to result in continuous reinforced (brittle) and unreinforced (ductile) regions extending along the entire length of the extrusion. As illustrated by Ashby et al. (1989), the benefits of extrinsic toughening can be maximized by employing ductile phase reinforcements with, (a) a high elastic modulus, (b) a high yield strength to elastic modulus ratio, and (c) a large volume fraction. In view of these considerations, three different types of extrinsically toughened composites were fabricated: (a) composites toughened with a low

volume fraction of a low yield strength ductile reinforcement such as commercial purity Al, (b) composites toughened with a large volume fraction of low yield strength commercial purity aluminum, and (c) composites toughened with a relatively large volume fraction of high strength aluminum alloy with flow strength several times the flow strength of commercial purity aluminum. Extrinsic toughening mechanisms that are expected to be operative during the dynamic deformation and failure of these composites include ductile tearing of the tough ductile phase, crack blunting, crack pinning and crack bridging in the wake of the crack, crack deflection, and energy absorption by inelastic interfacial decohesion.

The present study focuses on investigating the dynamic deformation and fracture characteristics of these novel extrinsically toughened particle reinforced aluminum composites. A split Hopkinson pressure bar apparatus is utilized for obtaining the high strain-rate compression behavior, whereas the dynamic fracture characteristics of these composites is evaluated by employing three point bend specimens loaded in a modified Hopkinson bar apparatus. In some of the dynamic fracture tests crack propagation gages are used to investigate the interaction of the propagating cracks with the extrinsically toughened material microstructure. Extensive optical and scanning electron microscopy is used to elucidate the micro- and the macro-damage mechanisms operative under dynamic compression and during dynamic fracture of these composites.

2. Material microstructure of extrinsically toughened composites under investigation.

Three different extrinsically toughened microstructures are investigated in the present study. The 7093/SiC/15p composite represents the base material for each composite. The nominal composition of the 7093/SiC/15p base material is 9 Zn, 2.2 Mg, 1.5 Cu, 0.14 Zr, 0.1 Ni and balance Al, reinforced with 10 μm average size SiC particles. The steps involved in powder processing of the base composite involves blending powders of the pre-alloyed 7093 aluminum with SiC particulates and then cold iso-statically pressing (CIP) the blend into a solid compact. CIP consists of placing the powder in a flexible mold which is then pressurized hydrostatically in closed chamber (Lewandowski and Liu, 1988).

The *extrinsic toughening* of the DRA composites is achieved by adding either large aluminum particles with a typical size of 10 mm, or relatively fine aluminum powder to the powder blend. Table 1 lists the different material compositions of the composites employed under the study. After the specified additions and consolidation, the billets are extruded to an extrusion ratio of 22:1 to produce composites with cross-sectional dimensions of 25.4×76.2 mm. The LDP3 composite was extruded a second time to yield final cross-sectional dimensions of 5×60.325 mm. Fig. 1 shows optical micrographs of the extrinsically toughened microstructures. The large ductile phase (LDP) additions are elongated in the extrusion direction and appear as elongated ellipsoids in Fig. 1(a), whereas the small ductile phase additions appear as dark spots in the micrographs shown in Fig. 1(b). Note that the large dark regions in Fig. 1(b) represent the SiC_p reinforcements.

Table 1
Composition and volume fraction of ductile phase reinforcements in the SDP1, LDP2 and LDP3 composites

CWRU material ID	Type of ductile phase addition	Quantity (vol%)
Small ductile phase 1 (SDP1)	Small c.p. Al — low strength powder	10
Large ductile phase 2 (LDP2)	Large c.p. Al — low strength unalloyed granulated particle	25
Large ductile phase 3 (LDP3)	Large alloyed Al — high strength CU50 granulated particle	10

2.1. Heat treatment

The heat treatment of 'precipitation hardenable' aluminum alloys is basically a three step process:

(i) Solution heat treatment: heating the alloy to a suitable temperature and holding that temperature long enough to cause one or more constituents to enter into solid solution.
(ii) Quenching: development of super saturation.
(iii) Age hardening: precipitation of solute atoms at room temperature (natural aging) or at moderately elevated temperature (artificial aging or precipitation heat treatment). Depending on the aging time the alloy after heat-treatment can be under-aged or over-aged.

Christman and Suresh (1988) have investigated the effects of aging time on precipitate growth in 2124 Al alloy SiC whisker reinforced composites. They observed that a large thermal contraction mismatch results in between the aluminum matrix and the SiC whisker reinforcement results in a large number of misfit dislocations in the composites. These dislocations serve as sites for preferential precipitate nucleation during the aging process and facilitate the attainment of peak matrix hardness at a much earlier time in the composites when compared to the control alloy. Also, the accelerated aging of the composites result in relatively large precipitates in the composites as compared to the control alloys in

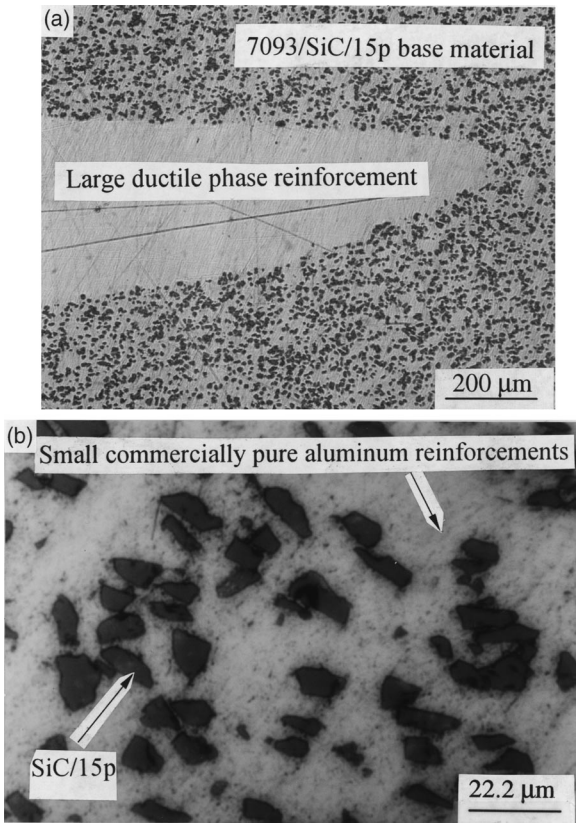

Fig. 1. (a) Optical micrographs of LDP2(L) composite. The large grey area is the ductile phase reinforcement surrounded by the 7093/SiC/15p discontinuously reinforced aluminum (base material). (b) A higher magnification view of the SDP1 composite. The average size of the SiC particles is 10 μm.

the over-aged condition. On the other hand, for an Al–Zn–Mg–Cu alloy (7xxx series) SiC_p reinforced MMC in an over-aged condition, Hong and Gray (1992) have observed the precipitates to be consistently smaller in size as compared to the precipitates in the control alloy with a similar heat treatment. They attributed this to the formation of MgO particles at the Al/SiC interface and to the formation of Mg_2Si precipitates in the matrix of the composite. The formation of magnesium rich precipitates results in the depletion of Mg atoms in the matrix of the composite, which in turn leads to deceleration of aging kinetics in the particle reinforced Al–Zn–Mg–Cu composites. Moreover, Hong and Gray (1992) have reported the yield stress of under-aged/over-aged 7xxx aluminum alloy composites to be consistently lower/higher than the 7xxx aluminum control alloys with a similar heat treatment.

In view of the aforementioned studies and the fact that the control alloy employed in the present investigation is a 7xxx series aluminum alloy, the composites utilized in the present investigation were heat treated in accordance to T7E92. The T7E92 heat treatment results in as lightly overaged condition of the composite and is expected to maximize the yield strength. This heat-treatment comprises solution heat treating for 4 h at 490°C, cold water quench, and aging for 24 h at 120°C plus 8 h at 150°C.

3. Quasi-static and dynamic compressive strengths of the extrinsically toughened particle reinforced aluminum composites.

3.1. Specimen preparation

Fig. 2 shows a schematic of the extrinsically toughened composites with the large and small ductile phase reinforcements. Two different sets of specimens were utilized for the quasi-static compression tests. The first set of specimens was machined such that the direction of the longitudinal extrusion axis is aligned with the direction of the compression loading. In this orientation the ductile phase reinforcements appear as elongated ellipsoids on the loading face. For convenience the specimens in this orientation are labeled as L specimens. The second set of specimens was machined such that the transverse extrusion axis is aligned with the direction of compressive loading. In this case the ductile phase reinforcement appear as thin streaks on the loading face. These specimens are labeled as T specimens. Note that the L and T specimens contain different volume fraction of the ductile phase reinforcement. This is primarily due to the in-homogeneous distribution of the ductile phase reinforcement in the billet after the extrusion process. This is also clearly evident from the schematic of the billet shown in Fig. 2, where the S–L cross-section is very different from the S–T cross-section. For all the specimens tested in the present investigation the L specimens has a higher volume fraction of the ductile phase reinforcement as compared to the T specimens. Besides the tests on the extrinsically toughened composites, the quasi-static and dynamic compression tests were also conducted on the 7093 Al control alloy and commercial purity aluminum.

The dimensions of the specimens utilized in the quasi-static uniaxial compression experiments were 6.35 mm in diameter and 5.0 mm in thickness (L/D ratio of 0.8). For the dynamic uniaxial compression tests the specimens were 10.16 mm in diameter and 5.0 mm in thickness. A L/D ratio of 0.5 is employed for the dynamic tests in order to minimize the effects of lateral inertia (Follansbee, 1985).

3.2. Quasi-static compression experiments

The quasi-static compression tests were performed on a Schenck Pegasus servo-hydraulic testing machine under displacement control. During the compression tests the average strain rate in the specimens ranged from 0.004 to 0.006 s^{-1}. Prior to the tests the loading faces of the specimens are

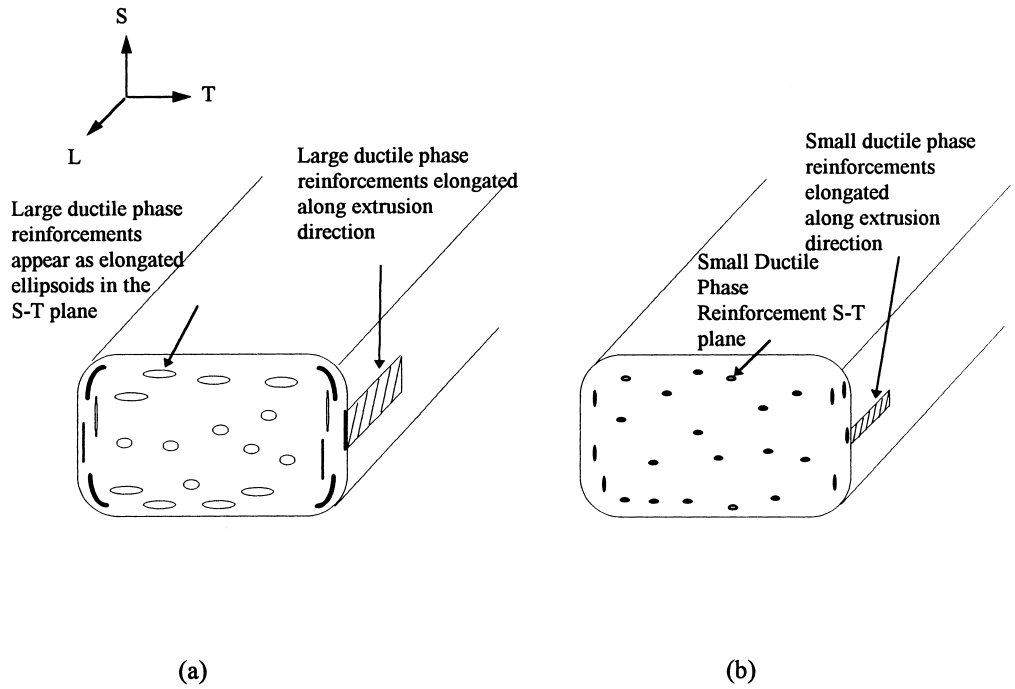

Fig. 2. Schematic of composite billet. (a) LDP2(L) composite — large ductile phase reinforcement shown as elongated ellipsoids after extrusion. (b) SDP1 — small ductile phase reinforcement shown much larger in the schematic than actual size.

lapped ground and for parallelism and flatness, and lubricated with molybdenum grease so as to avoid frictional end effects that may lead to barreling of the specimens.

Fig. 3 shows the quasi-static true-stress true-strain curves for the three extrinsically toughened composite microstructures employed in the present investigation. Also included in Fig. 3 are the true-stress true-strain curves for 7093 Al alloy (control alloy) and commercial purity aluminum. Five important deductions can be made from these results.

- Firstly, all materials tested under quasi-static compression in the present investigation do not exhibit a sharp yield point. Instead, yield occurs by a gradual transition from linear elastic to non-linear plastic behavior. The 7093 Al alloy and the commercial purity aluminum are well known to exhibit such a behavior (Khan and Huang, 1995). However, in the case of the composites, because of the large mismatch between the elastic stiffness of the SiC particulates and the metal matrix, there is an uneven partitioning of load between the matrix and the reinforcing particles. The stress supported by the hard reinforcing particles is much higher than that supported by the matrix. As a result, even at global stress levels much below the yield stress of the matrix, the stress in the vicinity of the particle–matrix interface is high enough to cause the matrix to yield locally. With a further increase in load, global yielding of the composite occurs by the spread of the local yield points in the matrix, resulting in the absence of a sharp global yield point for the composite.
- Secondly, all composites with the exception of LDP2(L) exhibit higher flow stress levels when compared to the control alloy, at all levels of the plastic strains. The reasons for this can be best understood by composite strengthening theories which include (i) load transfer between the matrix and the hard reinforcement phase (ii) presence of higher dislocation density in the matrix due to the elastic mismatch between the matrix and the reinforcement particulates, and (iii) precipitation

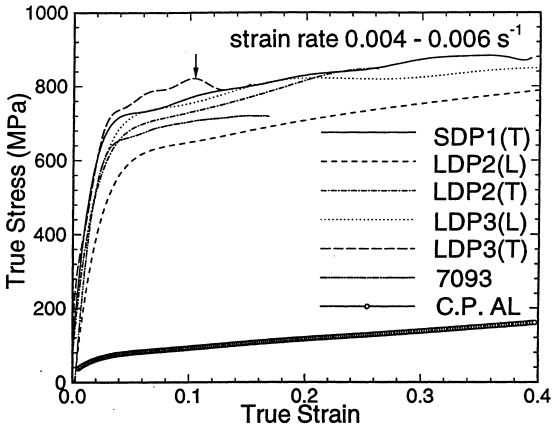

Fig. 3. Comparison of the quasi-static true-stress versus true-strain curves for the SDP1, LDP2, and LDP3 composites, the 7093 aluminum alloy and commercial purity aluminum. The alloyed ductile phase reinforced composite (LDP3) exhibited the highest yield strength.

hardening in particulate reinforced systems (Christman et al., 1989). The exceptional lower yield stress of LDP2(L) is due to commercially pure aluminum being used as the ductile phase reinforcement. Since commercial purity aluminum has a much lower flow stress as compared to the 7093 Al control alloy, it leads to a relatively lower yield stress for the LDP2(L) composite.

- Thirdly, for all the three extrinsically toughened composites, the *T* samples display a higher yield stress when compared to the *L* samples. The reason for this can be attributed to the higher volume fraction of the ductile phase reinforcement in the *L* samples as compared to the *T* samples. The higher volume fraction of the ductile phase reinforcement in the extrinsically toughened composites leads to a lower macroscopic flow strength of the composite since the ductile phase reinforcements have a lower flow strength as compared to the DRA material. Since the LDP3(T) composite has a large volume fraction of relatively high strength ductile phase reinforcement, the composite yield strength is highest for the LDP3(T) composite. The vertical arrow shown in the stress–strain curve of the LDP3(T)specimen (Fig. 3) denotes the strain at which the LDP3(T) composite fractures during dynamic compression.
- Fourthly, in all the deformed extrinsically toughed composites, slip lines were observed at 45° to the loading direction. This indicates a shear mode of failure of the composites during dynamic compression.
- Fifth, the strain-hardening-rate for the composites is greater than that observed in the 7093 Al control alloy and the commercially pure aluminum. This enhancement in the composite strain hardening characteristics can be attributed to, (a) the development of constrained plastic flow due to the presence of hard reinforcement particles in the ductile matrix, (b) increase in the initial dislocation density in the composites as compared to the unreinforced alloys due to the thermal expansion mismatch between the matrix and the reinforcement particles, and (c) smaller size precipitates in the composites as compared to the 7093 Al control alloys due to the difference in aging kinetics of the composite and the matrix (Hong and Gray, 1992). The smaller size precipitates offer a greater resistance to dislocation motion in the matrix of the composites resulting in their higher strain hardening rate. Also, as observed from Fig. 3, the strain-hardening-rate for the composites decrease at higher levels of plastic strain. This behavior can be attributed to material softening due to the accumulation of damage in the composites with increasing levels of plastic strain. Also, in metal

matrix composites, at the higher levels of plastic strain, dislocation tangles are known to build up enough energy to break free (Walkup, 1994) leading to a smaller resistance to dislocation motion and hence to a lower strain hardening rate.

4. Behavior under dynamic compression

4.1. Experimental configuration

In the present investigation the Split Hopkinson Pressure bar (SHPB) is used to investigate the high strain rate compressional behavior of the extrinsically toughened DRA composites in 100 to 10,000 s^{-1} strain rate range. The schematic of the experimental configuration is shown in Fig. 4. Details of the SHPB experimental technique can be found in Follansbee (1985). The experimental technique involves two elastic bars known as the incident and the transmission bars, and a dynamic loading device, usually a pneumatically driven gas gun with an elastic striker bar, which imparts to the incident bar a uni-axial stress pulse. The magnitude of the incident pulse is directly proportional to the velocity of the striker bar and the duration of the pulse is equal to the round-trip time of an elastic longitudinal wave in the striker bar. Striker bars of three different lengths 609.6 mm (2 ft), 304.8 mm (1 ft), and 228.6 mm (9 in.) were employed in the present investigation to obtain incident stress pulses with three different pulse durations. Maximum striker bar velocities were restricted to approximately 100 m/s, limited by the yield stress of maraging steel (tempered to a yield stress of approximately 2500 MPa) used to fabricate the pressure bars.

When the striker bar impacts the incident bar, an elastic compressive pulse propagates along the incident bar, and is partly transmitted to the transmission bar by the specimen sandwiched between the two bars, and is partly reflected as tension back into the incident bar. The specimen then undergoes dynamic elastic–plastic deformation. From the transmitted pulse, the stress in the sample can be calculated using the strain record obtained through a strain gage placed appropriately on the transmission bar, and from the reflected pulse, the strain in the sample can be obtained by integrating the strain measured by a strain gage suitably attached to the incident bar. Two strain gages are used at

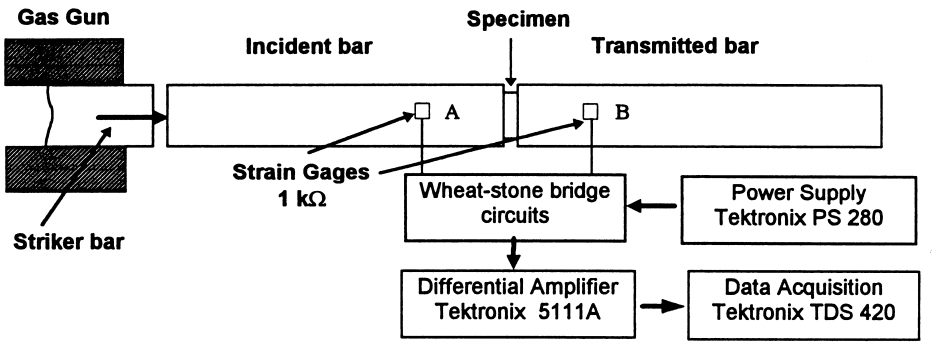

Fig. 4. Schematic of split hopkinson pressure bar apparatus (SHPB) for the dynamic compression experiments. The specimen is sandwiched between the incident bar and the transmitted bar.

each of the strain-gage station on the incident and the transmitter bars to eliminate bending contributions.

The initial part of the stress–strain relation is often neglected, as the stress state in the sample is inhomogeneous. Elementary calculations based on one-dimensional elastic waves in the bars provide an estimate of the sample strain rate,

$$\dot{\varepsilon}(t) = -\frac{2C_0}{L_0}\varepsilon_R = \frac{2C_0}{L_0}(\varepsilon_i - \varepsilon_t) \tag{1}$$

where L_0 is the undeformed length of the sample, C_0 is the longitudinal wave velocity in the pressure bars, and ε_R, ε_i, and ε_T are the time-dependent reflected, incident and transmitted strains, respectively. The axial stress in the sample, σ, is obtained from the balance of total force between the sample and the transmission bar,

$$\sigma(t) = E_0\frac{A_0}{A}\varepsilon_T(t) \tag{2}$$

where A is the area of cross section of the specimen, and A_0 is that of the transmission bar whose Young's Modulus is E_0.

Theoretically a rectangular input loading pulse is sent into the incident bar. However, because of the presence of lateral inertia the incident square pulse is dispersed giving rise to the oscillations observed to be riding the square incident pulse. In order to minimize the effects of dispersion and hence the oscillations in the input stress pulse, a damper (a 400 μm thick OFHC copper disk) is placed in between the impact faces of the striker and the incident bars (Nemat-Nasser et al., 1991). The presence of the damper changes the incident square stress profile to a bell shaped profile. The initial ramp in the modified bell shaped stress pulse not only decreases the effects of dispersion but also precludes the sudden loading of the specimen leading to attainment of homogeneous deformation conditions at a much smaller level of plastic strain in the specimen.

4.2. Experimental results and discussion

4.2.1. Dynamic compression behavior of 7093 Al alloy

Fig. 5 shows the dynamic compressive true-stress versus true-strain curve for the 7093 Al control alloy. The response of the 7093 Al alloy is practically insensitive to strain rate in the range 0.004–207 s^{-1}. However, there is a noticeable increase in the sensitivity of flow stress to strain rate as the strain rate is increased to 4500 s^{-1}. In the strain-rate range of 0.004 to 207 s^{-1} the 7093 control alloy shows appreciable strain hardening. However, at higher levels of strain rate, i.e. $\dot{\varepsilon} \sim 4500$ s^{-1}, the material strain hardening and material strain rate sensitivity is compensated by strain softening. Possible reasons for strain softening include, (a) material softening due to the accumulation of damage, and (b) thermal softening due to adiabatic heating arising from conversion of plastic work to heat. An indication of the accumulation of damage can be deduced from the precipitous fall in the stress–strain curve for the specimen tested at 4501 s^{-1} (indicated by a vertical arrow on the curve). The possible effects of thermal softening on the material's flow stress are discussed in Section 4.3.

4.2.2. Dynamic compression behavior of SDP1(T) composite

Fig. 6 shows the true-stress versus true-strain curves for SDP1(T) at strain rates ranging from 0.005 to 4983 s^{-1}. The large undulations in the dynamic stress–strain response, especially at small levels of plastic strains, are an artifact of wave dispersion due to lateral inertia. The quasi-static flow stress of the SDP1(T) composite is higher than the quasi-static flow stress for the 7093 Al alloy (control alloy) at all

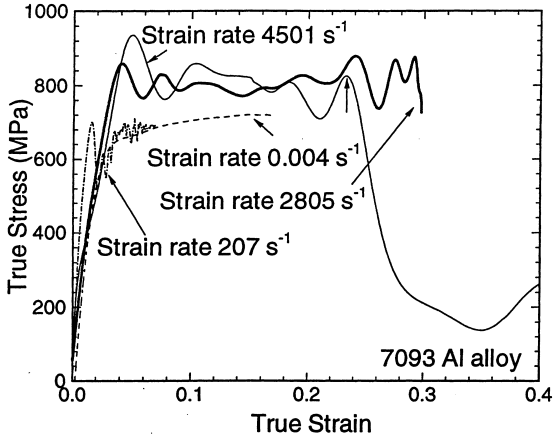

Fig. 5. True-stress versus true-strain curves for 7093 aluminum alloy depicting the higher strain rate sensitivity of flow stress in the higher strain rate regime (4501 s^{-1}) as compared to the low strain rate (207 s^{-1}) regime.

levels of plastic strains. This is expected because of the presence of hard reinforcing particles in the composites, and the presence of a relatively small volume fraction of the commercial purity aluminum ductile phase reinforcement in the SDP1 composites. However, the dynamic flow stress of the SDP1(T) composite is much lower than the dynamic flow stress of the 7093 Al control alloy at comparable levels of strain-rate. The possible reasons for this behavior can be attributed to the strain softening mechanisms activated in the composite during the dynamic loading, i.e., (a) material softening due to damage accumulation and growth, and (b) thermal softening of the composite due to adiabatic heating. It can be argued that material softening due to damage nucleation and growth is the most likely source for the observed strain softening behavior since the matrix of the SDP1(T) composite comprises 7093 Al alloy and any thermal softening effects are expected to influence the flow response of the SDP1 composite and the 7093 Al control alloy equally. Furthermore, the dynamic flow stress of the SDP1(T) composite, at all levels of plastic strains and plastic strain rates employed in the present investigation, is observed to be lower than the quasi-static flow stress of SDP1(T). A possible reason for this can be

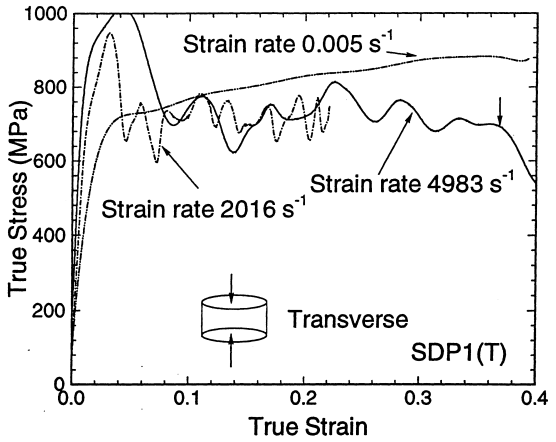

Fig. 6. True-stress versus true-strain curves for SDP1(T) composite.

attributed to, (a) thermal softening during the dynamic deformation process and, (b) the loss in the material's strain-rate sensitivity of flow stress in the extruded particle reinforced composites due to the already work hardened matrix (Ramesh and Coates, 1992).

It should be noted that at the lower strain rates no macroscopic damage is observed in the deformed specimen. However, on a much finer scale, damage in the form of cracking along the particle/matrix interface (Hong et al., 1993) is expected to be present. The onset and growth of damage within the composite can be inferred from the precipitous fall in the dynamic stress–strain curve at a strain rate of 4983 s^{-1} due to the fracture of the specimen.

4.2.3. Dynamic compression behavior of LDP2 composites

Figs. 7 and 8 show the dynamic stress–strain curves for the LDP2(L) and LDP2(T) composites, respectively. The overall trends in the dynamic stress–strain behavior for the two composites are quite similar to those observed for the SDP1(T) composite. However, the dynamic flow stress levels for the LDP2(L) and LDP2(T) composites are much lower than those obtained for the 7093 Al control alloy at comparable levels of plastic strain rates. Moreover, the quasi-static stress–strain curves for the LDP2(L) and LDP2(T) composites show strain hardening at all levels of plastic strain, whereas the dynamic stress–strain curves are relatively flat. The absence of strain-hardening in the dynamic response of these composites can be attributed to the combined effects of material and thermal softening which are activated during the dynamic deformation process. Fig. 9 shows a micrograph of the deformed specimen of LDP2(L) composite tested at strain rate of 4317 s^{-1}. Matrix cracking is clearly visible in the deformed specimen. Such matrix cracking is not observed in specimens deformed at the lower strain rates. It should also be noted that the quasi-static as well as the dynamic flow stress levels for the LDP2(L) and LDP2(T) composites are lower than those obtained for SDP1 composites at comparable levels of plastic strain rates. This can be attributed to the higher volume fraction of commercially pure aluminum present in the LDP2(L) and LDP2(T) composites as compared to the SDP1(T) composite. Also, the flow stress levels for LDP2(L) are consistently lower than the flow stress levels for LDP2(T) at all levels of plastic strain. Again this is to be expected because of the presence of a higher volume fraction of commercially pure aluminum present in LDP2(L) composite as compared to the LDP2(T) composite.

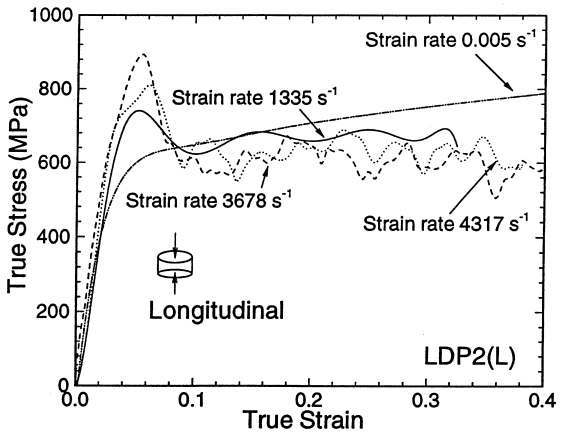

Fig. 7. True-stress versus true-strain curves for LDP2(L) composite.

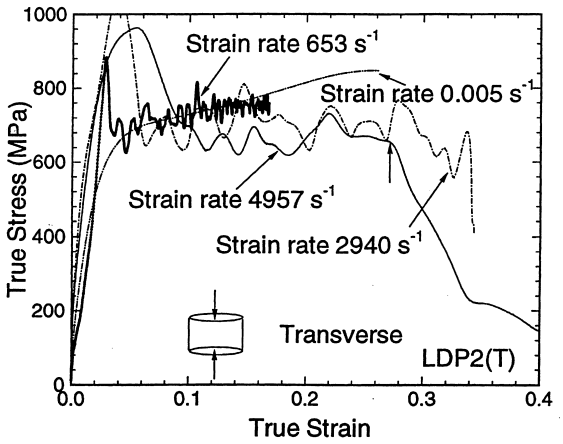

Fig. 8. True-stress versus true-strain curves for LDP2(T) composite.

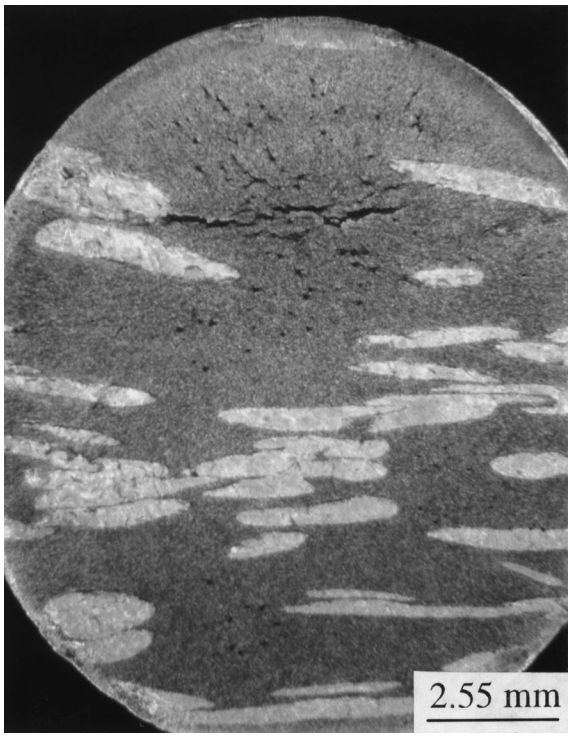

Fig. 9. A deformed LDP2(L) specimen after dynamic compression. Note matrix cracking in the brittle 7093/SiC/15p base material away from ductile phase reinforcement.

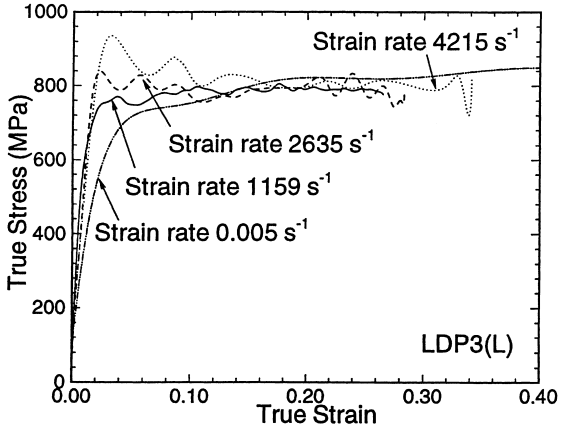

Fig. 10. True-stress versus true-strain curves for LDP3(L) composite. Note that the composite exhibits strain hardening under quasi-static compression and little or no strain hardening under dynamic compressive loading.

4.2.4. Dynamic compression behavior of LDP3 composites

Figs. 10 and 11 show the quasi-static as well as the dynamic stress–strain behavior of LDP3(L) and LDP3(T) composites, respectively. To minimize the effects of dispersion on the dynamic stress–strain curves for these composites, a copper damper was placed between the striker bar and the incident bar. The benefits derived from the use of the copper damper can be inferred from the absence of any large oscillations in the dynamic stress–strain behavior. The quasi-static flow stress levels for the LDP3(L) and LDP3(T) composites are observed to be higher than those measured for either the 7093 Al control alloy or the SDP1(L), LDP2(L) and LDP2(T) composites. This behavior is to be expected because of the presence of a large volume fraction of ductile phase reinforcement with a much higher flow strength level as compared to the commercially pure aluminum reinforcements employed in the SDP1(T), LDP2(L) and LDP2(T) composites. It is also interesting to note that unlike the case of the SDP1(T), LDP2(L) and LDP2(T) composites the dynamic yield stress of the LDP3(L) and LDP3(T) composites

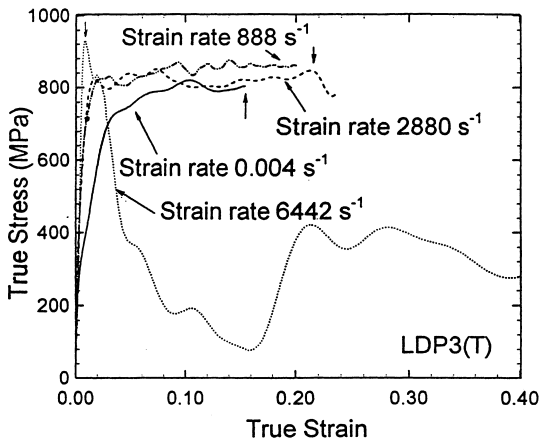

Fig. 11. True-stress versus true-strain curves for LDP3(T) composite exhibiting strain hardening at strain rates of 0.004 and 888 s^{-1}, strain softening at 2880 s^{-1} and fracture of the specimen at 6442 s^{-1}.

are higher relative to their quasi-static flow stress levels. This indicates a much lower level of damage in the LDP3(L) and LDP3(T) composites as compared to the SDP1(T) and the LDP2(L) and LDP2(T) composites. Moreover, the dynamic flow stress levels for the LDP3(T) composite, at the various strain rates employed in the present investigation, are higher than those obtained for the LDP3(L) composite. The LDP3(L) composite yields at 780, 800 and 840 MPa at strain rates of 1159, 2635 and 4215 s^{-1}, respectively, whereas, the LDP3(T) composite yields at approximately 830 and 840 MPa at strain rates of 888 and 2880 s^{-1}, respectively.

Moreover, the dynamic flow stress curves for the LDP3(T) composite shows strain hardening at a strain rate of 888 s^{-1}, and strain softening at a strain rate of 2880 s^{-1}. On the other hand, the LDP3(L) composites consistently show negligible strain hardening at all levels of plastic strain rates. The possible reasons for this behavior can be attributed to the greater rate of damage accumulation in the LDP3(L) composites as compared to the LDP3(T) composites. For example, at a strain rate of 2880 s^{-1} the LDP3(T) specimen is observed to fracture at a plastic strain of about 0.22 whereas at the strain rate of 6442 s^{-1} the specimen fractures at approximately the yield strain of the composite.

4.3. Estimation of temperature rise during dynamic compression

To estimate the effect of thermal softening on the flow stress behavior, the increase in temperature during the dynamic deformation process was estimated by assuming that all of the plastic work is converted into heat,

$$\Delta T = \frac{\bar{\sigma}\bar{\varepsilon}^{p}}{\rho c_p} \tag{3}$$

where ΔT is the temperature rise; $\bar{\sigma}$ and $\bar{\varepsilon}^{p}$ are the equivalent stress and the equivalent plastic strain, respectively; ρ is the mass density and c_p is the specific heat of the material. The highest temperature rise was estimated to be 84°C for the LDP3(L) composite specimen at a strain rate of 4215 s^{-1}. Using the thermal softening data on aluminum alloys from the ASM Handbook, the 84°C increment in the specimen temperature corresponds to a drop in yield stress of approximately 39 MPa. Even though this drop in flow stress corresponds to 5% of the yield stress, it still represents a significant fraction of the total strain softening observed in the experiments. Hong et al. (1993) have also identified thermal softening as one of the possible mechanisms responsible for the loss in the dynamic material strength of metal matrix composites.

4.4. Summary of quasi-static and dynamic compression tests

Fig. 12 summarizes the dynamic yield stress as a function of the applied plastic strain rate for the various materials investigated in the present study. In this plot the flow stress (measured at a fixed plastic strain of 6%) is plotted against the logarithm of applied plastic strain rate. The 6% plastic strain is chosen so as to de-couple the effects of strain rate hardening and strain-softening resulting from the combined effects of thermal softening and damage accumulation (both of which become important only at higher levels of plastic strains). Moreover, a smaller value of plastic strain was not chosen so as to avoid uncertainties in the flow stress levels due to wave dispersion. The observations deduced from the plot are as follows. First, in the monolithic alloy it is observed that there is reduced strain rate sensitivity beyond strain rates of 10^3 s^{-1}. A possible reason for this could be that the dislocation generation rate does not increase further with increasingly higher levels of strain rates in the high strain rate regime (Hong et al., 1993). Secondly, in the high strain rate regime the flow stress of both the SDP1 and LDP2 composites is lower than the flow stress of the monolithic 7093 Al control alloy. A possible

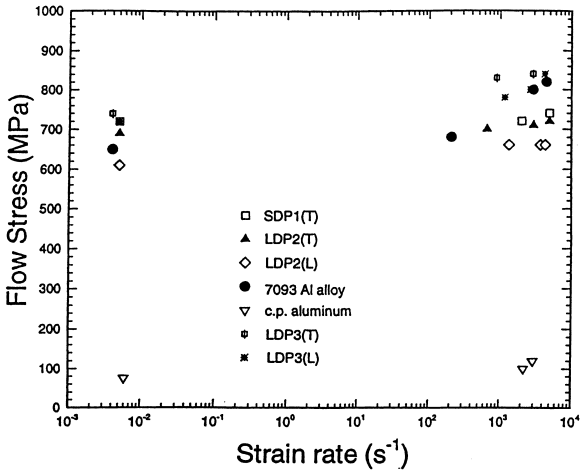

Fig. 12. Summary of the dynamic compression tests showing flow stress versus logarithm of the applied strain-rate at 6% plastic strain.

reason for this can be attributed to the presence of commercially pure aluminum as a ductile phase reinforcement in the SDP1 and the LDP2 composites. On the other hand, the LDP3 composite shows the highest level of flow stress at all levels of strain rates employed in the present study. It should be noted that besides having a high strength Al alloy as a ductile phase reinforcement for the LDP3 composites, the extrusion ratio for LDP3 was higher as compared to the SDP1 and the LDP2 composites evaluated in the present study. Thirdly, there is a loss of strain rate sensitivity of the SDP1, LDP2, and the LDP3 composites as compared to the monolithic 7093 Al alloy (control alloy). A possible explanation for this could be due to the substantial work hardening of the composite during the extrusion process which makes it difficult to generate additional dislocations at higher levels of plastic strain rates (Ramesh and Coates, 1992). Also, quenching during the heat treatment process, results in the generation of additional dislocations due to the coefficient of thermal expansion mismatch in the composite, which can contribute to saturation of the dislocation density within the composite.

5. Dynamic fracture characteristics of the extrinsically toughened particle reinforced metal matrix composites

Recently, there has been a resurgence of interest in the study of interfacial fracture mechanics, particularly for bi-materials in which one of materials is brittle and remains elastic while the other is ductile and can deform plastically. Examples of such situations arise during crack growth in metal-matrix composites, layered metal-ceramic material systems, and structural steels in which iron–carbon inclusions are the brittle phase.

Preliminary investigations of crack growth in multi-phase material systems with a two-dimensional layered ductile-brittle architecture and for which the ductile phase is considered as an elastic–plastic material, have shown that the effects of plastic flow and interface strength on the overall toughness of multiphase materials is quite complex. In elastic–plastic deformation of ductile layers may have only a moderate effect on the toughness of such systems since the ductile layer is constrained between hard elastic layers. Hence, the degree of plastic straining and energy absorption are limited. For example, Shaw et al. (1996) have explored ways of toughening ceramics by adding sandwich metallic layers

transverse to the plane of a crack, with the interfacial strength sufficiently high for crack not to deflect along the interface. Two competing modes were observed and modeled: (i) fracture by coplanar crack growth within successive ceramic layers ahead of the initial crack, and (ii) multiple cracking within the ceramic layers. It was found that plastic yielding of the metal layers encourages single, coplanar crack growth instead of multiple cracking. This result is surprising because of the single crack pattern is the low-energy mode, and the multiple crack pattern is the high energy mode (Siegmund et al., 1997).

One of the primary objectives of the present investigation is to examine the dynamic fracture characteristics of extrinsically toughened discontinuously reinforced composites in which the plane of crack growth is approximately perpendicular to the ductile/brittle interface. The issues of particular interest are, (a) develop an understanding of the conditions under which a crack will propagate across the interface as opposed to when it will be deflected into the interface, and (b) the mechanisms of energy absorption/toughening which are operative during the dynamic crack propagation event. Although there has been some experimental work on dynamic crack propagation in the plane a bimaterial interface (Lambros and Rosakis, 1995; Singh and Shukla, 1996; Kavaturu and Shukla, 1998), to the authors knowledge no results have been reported in the open literature which addresses the key features of dynamic crack growth in a direction perpendicular to the bi-material interface.

5.1. Experimental configuration for dynamic fracture experiments: modified Hopkinson bar apparatus

Fig. 13 shows the schematic of the experimental configuration employed to investigate dynamic fracture of the extrinsically toughened composite microstructures. The experiment involves the loading of a three point bend specimen by means of a modified Hopkinson bar apparatus (Bacon et al., 1994). The incident bar is made of 7075-T6 Al with a length of 1.5256 m and a diameter of 19.1 mm. The striker bar is made of the same material as the incident bar and has a length of 0.9017 m. The specimen end of the incident bar is provided with a radius of curvature of approximately 50.8 mm. The anvils supporting the specimen have a length span of 40 mm.

One of the advantages of using this configuration is that relatively large three point bend specimens can be used to evaluate the dynamic fracture characteristics of the composites under well characterized stress wave loading conditions. The use of a relatively large radius ofcurvature at the specimen end of the incident bar allows one-dimensional elastic stress wave propagation theory to be used in the interpretation of the experimental results. Bacon (1993) has studied the effects of tapering/rounding the incident bar end and has shown that the dispersion introduces an inadmissible error when the duration of the event under investigation is of the order of L/C, where L is the length of the taper and C is the longitudinal wave speed in the incident bar. For the present experiments the length of the taper is approximately 2 mm and hence the L/C ratio is approximately 0.33 μs. Since all time duration of

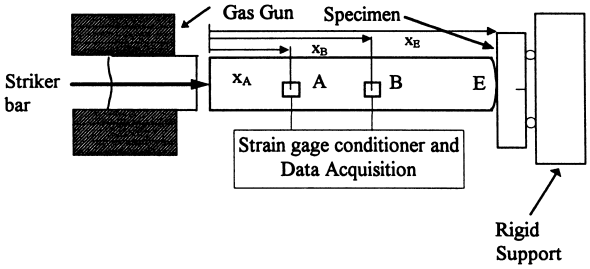

Fig. 13. Schematic of the modified Hopkinson bar configuration employed for conducting the dynamic fracture experiments. Upon firing the striker bar the three-point bend specimen is subjected to a well characterized stress wave loading pulse.

interest in the present experiment are much larger than 0.33 μs the errors due to the rounded incident bar end geometry are not expected to be significant. Moreover, by employing relatively long striker and incident bars allows input stress pulse of approximately 400 μs time duration to be generated. The relatively long duration of the stress pulse ensures that initiation and propagation of crack occurs within the time duration of a single input pulse. This greatly simplifies the interpretation of the experimental measurements and also allows load point force as well as the load point displacement to be inferred from measurements of the stress and the particle velocities at approximately the mid-span of the incident bar.

Strain gages are installed on the incident bar at positions A and B, which correspond to 350 and 750 mm from the impact end of the striker bar, respectively. Strain gages used have a gage factor of $2.07 \pm 1.0\%$ (WK-06-250BF-10C Measurements group). Two strain gages were used at each strain gage location to eliminate bending contributions. The strain gages are connected to differential amplifiers (Tektronix 5A22N) via wheat-stone bridges circuits. The amplified signal from the differential amplifier is recorded by using a high speed wide band width Tektronix oscilloscope model TDS 420.

The normal forces N_A and N_B at the two strain gage locations x_A and x_B, respectively, on the incident bar are given by

$$N_A(t) = A_0 E\varepsilon_A(t) \quad \text{and} \quad N_B(t) = A_0 E\varepsilon_B(t). \tag{4}$$

In view of the one-dimensional elastic stress wave propagation in the striker and the incident bars, and using the method of characteristics, the particle velocity $v_A(t)$, at the strain gage station A can be expressed as

$$v_A(t) = v_A(t_P) + \frac{1}{Z}\big[-N_A(t) - N_A(t_P) + 2N_B(t - T_{BA})\big] \tag{5}$$

where $t_P = t - 2T_{BA}$, $T_{BA} = (X_B - X_A)/C_0$ and Z is the acoustic impedance of the incident bar. Similarly, the particle velocity v_E, and the normal force N_E, at the loading point x_E can be expressed as

$$v_E(t) = \frac{1}{2}\big[v_A(t + T_{EA}) + v_A(t - T_{EA})\big] + \frac{1}{2Z}\big[N_A(t + T_{EA}) - N_A(t - T_{EA})\big] \tag{6}$$

$$N_E(t) = \frac{1}{2}\big[N_A(t + T_{EA}) + N_A(t - T_{EA})\big] + \frac{Z}{2}\big[v_A(t + T_{EA}) - v_A(t - T_{EA})\big] \tag{7}$$

where $T_{EA} = (x_E - x_A)/C_0$.

Using Eqs. (4)–(7), the load-point displacement $u(t)$, and the load-point force $F(t)$, can be expressed as

$$u(t) = \int_0^t v_E(\tau)\, d\tau \quad \text{and} \quad F(t) = -N_E(t), \text{ respectively.} \tag{8}$$

Lundberg and Henchoz (1977) have discussed the main sources of error in the two point strain measurement scheme employed in the present experiments. First, the equations of motion used in the present analysis assume one-dimensional wave propagation. However, during longitudinal stress wave propagation in elastic bars, three-dimensional effects commonly known as geometric dispersion are present. Secondly, Eqs. (4)–(8), require the precise locations of strain gages A and B. Any in-accuracy in the location of the strain gage results in the propagation of this error. The third source of error corresponds to the uncertainties in the physical properties of the incident bar material, i.e. the density of the bar, the longitudinal bar speed, and the elastic modulus. For error estimation purposes, an experiment was conducted without the specimen placed at the end of the incident bar, i.e. keeping the

load point end of the incident bar as a free end. The objective was to compare the known solution for force and particle velocity at the free end of the incident bar from the measurements of strains at the strain gage locations A and B. Using a longitudinal bar wave speed of 5100 m/s for 6065-T6 Al alloy, density of 2810 kg/m^3, and an elastic modulus of 73 GPa, the maximum error obtained in load-point force was approximately 6%.

Besides, the aforementioned sources of errors, the modified Hopkinson bar configuration for dynamic fracture shares some of the inherent problems associated with instrumented impact testing. Earlier work by Nakamura et al. (1986) has quantified the effects of material inertia in laboratory three-point-bend fracture specimens. Their work has suggested several avenues to minimize such effects. In particular, they have shown that the behavior of a dynamically loaded three point bend specimen can be characterized by a short time response dominated by discrete waves, and a long time response that is essentially quasi-static. At intermediate times, the global inertia effects are significant but the local oscillations at the crack tip are small due to kinetic energy being absorbed by the crack tip plasticity. Furthermore, to distinguish short time response from the long time behavior, they defined a transition time, t_τ, as the time at which the kinetic energy and deformation energy in the specimen are approximately equal. From this analysis they concluded that the effects of material inertia dominate prior to the transition time, but the deformation energy dominates at times significantly greater than t_τ. Thus, for $t \gg t_\tau$ inertia effects can be neglected and quasi-static models can be applied in the interpretation of the experimental results.

From the analysis of Nakamura et al. (1986), the transition time

$$t_\tau = D\Lambda\frac{W}{c_0}, \tag{9}$$

where W is the width of the specimen, Λ is a geometric factor, and D is a non-dimensional constant denoted by

$$D = t\frac{\dot{\Delta}}{\Delta}|_{t_\tau}. \tag{10}$$

In Eq. (10), Δ is the instantaneous load point displacement, and $\dot{\Delta}$ is the rate of load point displacement, both being evaluated at $t = t_\tau$.

For relatively, brittle specimens, which are of primary interest in the present study, the quasi-static analysis conditions can be met by minimizing t_τ. This can be achieved by (a) decreasing the applied displacement rate, i.e. by decreasing the impact velocity and/or employing a relatively low impedance incident bar instead of the conventional maraging steel bar employed in split Hopkinson bar apparatus, and (b) by decreasing the width of the specimen. In view of these considerations, in the present investigation a 6061-T6 Al alloy bar was used instead of the maraging steel bar and the impact velocity was limited to a maximum of 10 m/s.

To estimate the critical material toughness at crack initiation an approach similar to the one proposed by Plati and Williams (1975) is employed. In this approach the material toughness is defined by the equation:

$$G = \frac{U}{BD\phi}, \tag{11}$$

where U is the measured energy upto crack initiation, B is the specimen thickness, D is the specimen depth, and ϕ is a known function of span to depth ratio (L/D) and crack depth to specimen depth ratio (a/D).

5.2. Specimen geometry and notch orientation relative to material microstructure

All the dynamic experiments were conducted with the specimens in the T–S configuration. The T–S configuration was used to ensure that the propagating crack approaches the ductile phase reinforcement in a crack arrester geometry, i.e. the crack runs normally into the ductile interface. The anvils supporting the specimen had a length span of 40 mm. The specimens were machined from the original extrusion by using electro-discharge machining, and were 9 mm wide and 10 mm deep giving an L/D ratio of 4. Notch depths of either 3 or 5 mm were machined using a diamond wire saw of diameter 100 μm. The exact length of the notch was later measured by using a traveling microscope. For the specimen geometry employed in the present experiments, $L/D = 4$ and $a/D = 0.3$ or 0.5. The corresponding values for ϕ are 0.354 and 0.233, respectively.

5.3. Experimental results and discussion

5.3.1. Dynamic fracture characteristics of SDP1 and LDP2 composites

Fig. 14 shows the load-point force versus displacement curves for the 7093/SiC/15p + 10% small commercial purity aluminum composite (SDP1), and the 7093/SiC/15p + 25% large commercial purity aluminum composite (LDP2). The impact velocity for the experiment conducted on the SDP1 composite was 2.8 m/s and the impact velocity for the experiment conduct on the LDP2 composite was 4.4 m/s. The first peak in the force versus displacement curves for both the composites is due to inertia; the further rise in force until the attainment of the highest peak represents the time for crack initiation. Once the crack initiates, the load-point force falls sharply since the extension of the crack brings down the stiffness of the specimen. As seen from Fig. 14, the crack initiation time for the SDP1 and the LDP2 composites is quite similar. The energy absorbed by the composite upto crack initiation is approximately 2.25 J/cm^2. This is also to be expected since the notch resides completely in the 7093/SiC/15p base material in both cases. However, the dynamic crack propagation characteristics for the two composites are significantly different. In the case of the small ductile phase toughened composite (SDP1) the

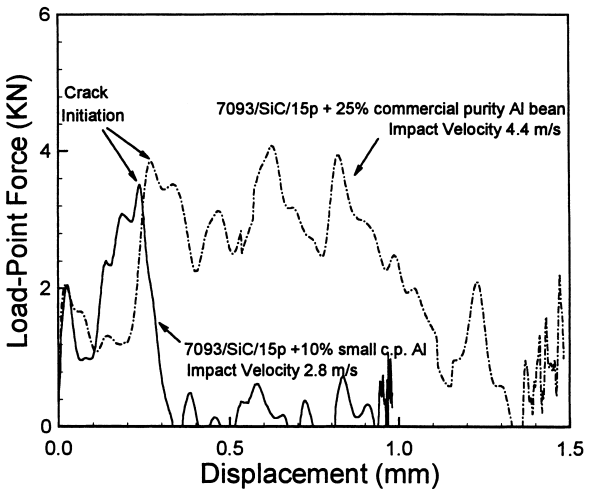

Fig. 14. Load-point force versus displacement curves for LDP2 and SDP1 composites. A larger area under the load-point force versus displacement curve for the large ductile phase reinforced composite indicates greater resistance during crack initiation and growth.

dynamic crack propagation is relatively straight with very little energy being absorbed during crack propagation. On the other hand, for the case of the LDP toughened composites (LDP2), the crack path is governed by several interactions the crack front has with the ductile phase reinforcements absorbs significantly more energy during crack propagation.

Fig. 15 shows the material microstructure ahead of the notch for the LDP2 composite. A number of ductile phase reinforcements can be observed ahead of the crack tip. The dashed line shows the path taken by the crack during dynamic fracture of the composite. The crack is observed to deflect sideways along the interface as it encounters the first ductile phase reinforcement. Failure of the ductile phase occurs by the tearing of the reinforcement ligaments in the wake of the crack. The ductile ligaments are observed to be plastically stretched and also show evidence of necking during the ductile tearing process. Also, during the tearing of the ductile ligaments, the ductile/brittle interfaces in the vicinity of the crack propagation path, are observed to delaminate. Each peak in the force–displacement curve after crack initiation, can be correlated to a particular extrinsic toughening mechanisms activated every time the cracken counters a LDP reinforcement in its propagation path.

Fig. 16(a) shows a SEM micrograph of the fracture surface for the LDP2 composite. Alternating layers of the ductile phase reinforcement and the SiC particle reinforced aluminum can be clearly seen. A closer look into the ductile phase reinforcement (Fig. 16(b)) shows that micro-void coalescence to be the predominant mode of failure in the large commercially pure aluminum reinforcements. Also, in the neighborhood of the ductile phase reinforcement layer there is evidence of some interfacial delamination as the crack enters and exits the ductile phase reinforcement. A close examination of the region

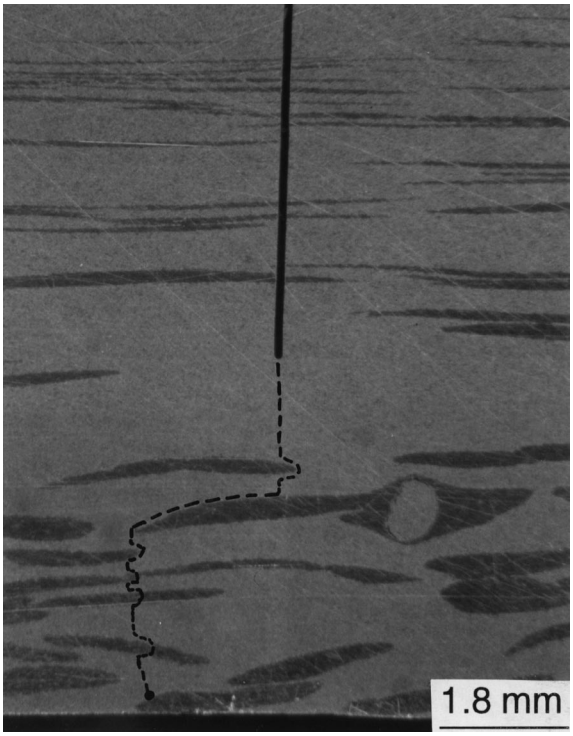

Fig. 15. Material microstructure ahead of the pre-machined notch for a typical LDP2 composite dynamic fracture specimen. The dashed line indicates the path taken by the crack during dynamic fracture. The failure mechanisms include ductile tearing of the large ductile phase reinforcement, crack deflection, and delamination of the ductile/brittle interface.

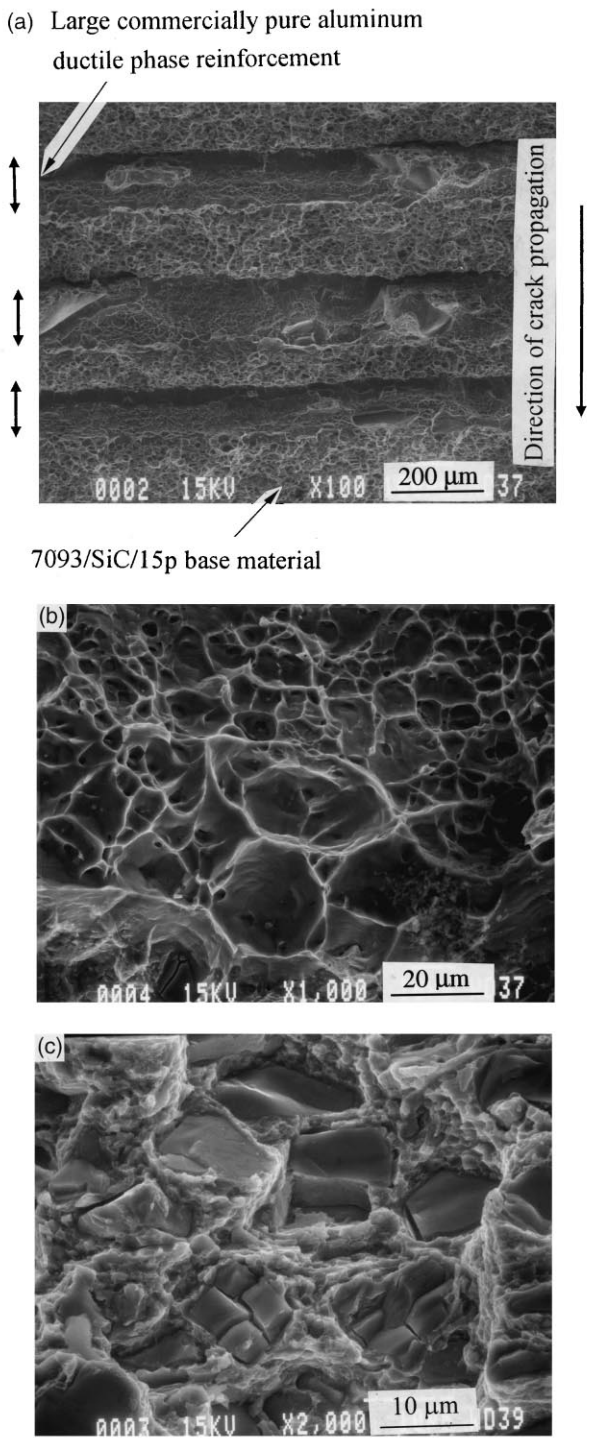

Fig. 16. (a) Micrograph showing typical fracture surface for LDP2 composite. Alternating layers of the ductile phase reinforcement and the 7093/SiC/15p base material can be easily identified. (b) A magnified view of ductile failure within a large commercially pure aluminum reinforcement. The ductile mode of failure is in part responsible for absorbing considerable amount of energy during the crack propagation phase. (c) A magnified view of failure in the 7093/SiC/15p base material showing the fragmentation of the brittle SiC reinforcement particle and its decohesion from the ductile matrix.

(Fig. 16(c)) in the vicinity of the crack path shows that the failure in the brittle particle reinforced region occurs by the nucleation and growth of micro-voids due to particle cracking and subsequent de-cohesion of the reinforcement particle from the surrounding matrix.

In order to investigate the effect of impact velocity on the dynamic fracture characteristics of the LDP2 composites, a few experiments were conducted at approximately half the impact velocity of the experiment described in Fig. 14. Fig. 17 shows the typical material microstructure ahead of the notch for the experiment conducted at 2.4 m/s. The corresponding load point force–displacement history is shown in Fig. 18. Crack arrest occurs after approximately 0.5 mm of load-point displacement. Fig. 19 is an optical micrograph showing the path taken by crack. As the crack approaches the very first ductile reinforcement layer it is observed to deflect parallel to the ductile/brittle interface leading to crack arrest. A close-up view of the region ahead of the arrested crack tip shows evidence of plastic deformation in the form of slip bands in the commercial purity Al reinforcement.

The aforementioned experimental results are consistent with the recent finite element simulations of Siegmund et al. (1997) for dynamic crack growth across interfaces between elastic and elastic-viscoplastic materials. They showed that for crack growth from a harder material phase into a more ductile phase with power law strain hardening, and with interface strength of approximately 25% of the material cohesive strength, the crack momentarily arrests at the interface but eventually propagates through it. Furthermore, they observed that for cases when the ductile phase was described by a combined power law hardening and enhanced strain-rate hardening, the crack speed in the elastic material plays the determining role in whether or not the crack penetrates the interface. When the crack approaches the interface at a speed which is high enough such that the local strain-rates in the vicinity

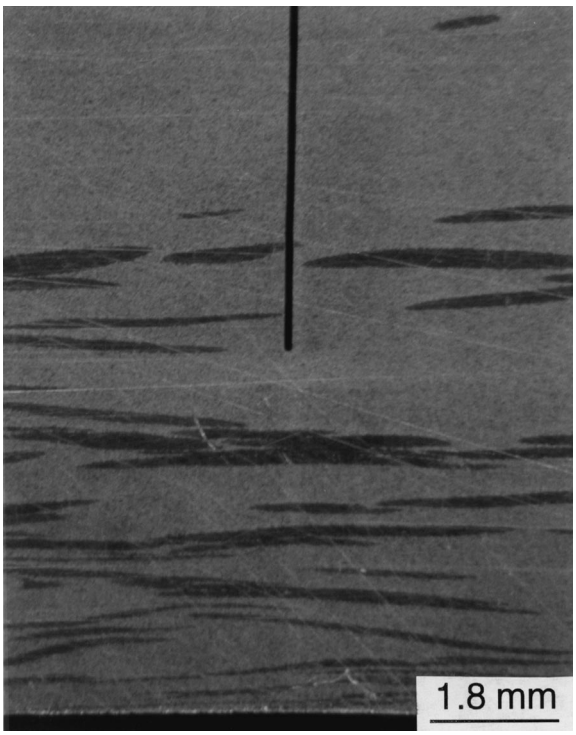

Fig. 17. Microstructure ahead of the pre-machined notch in LDP2 composite. The impact velocity was 2.4 m/s. The combination of low impact velocity and the cluster of ductile phase reinforcements lead to crack arrest.

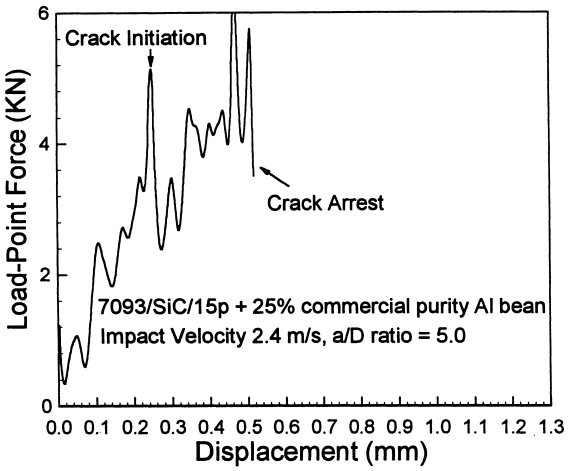

Fig. 18. Load-point force versus displacement curves during crack propagation and arrest (impact velocity 2.4 m/s). The highest peak in the force versus displacement curve indicates the point of crack initiation.

of the crack tip are higher than the critical strain-rate for transition from the power-law hardening to enhanced strain-rate hardening then the crack propagates through the ductile phase. On the other hand, if the crack tip speed is small such that the local strain-rates are lower than the transitional strain-rate then the softer material appears more 'ductile' and leads to crack arrest.

5.3.2. Dynamic fracture characteristics of LDP3 composites

In the present study, the majority of the dynamic fracture experiments on LDP3 composites were conducted with crack propagation gages (CPG) placed on the specimen surface. The motivation of using the CPGs was to understand the correlation between load point force and the crack tip velocity as the crack interacts with the ductile phase reinforcement. Micro-Measurement group's TK-09-CPA01-005/DP

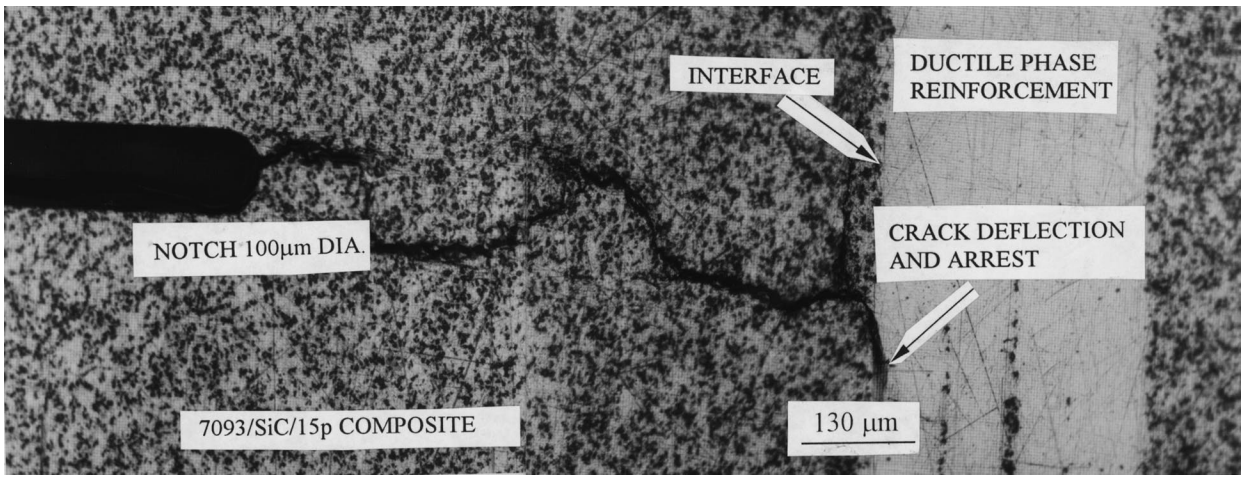

Fig. 19. Optical micrograph of crack arrest at the brittle/ductile interface (impact velocity 2.4 m/s). The crack runs in a zigzag pattern in the brittle phase before being arrested by crack deflection into the brittle/ductile interface.

crack propagation gages with 20 grid lines over a length of 5.1 mm were used. For recording the CGP voltage output a HP54542A digitizing oscilloscope was used with a sampling rate of 25 MSa/s. The first 8 V jumps, corresponding to the fracture of eight CPG wires closest to the notch, range from 5 to 10 mV. The final voltage jump (corresponding to the breakage of the 20th CPG wire) is of the order of 160 mV and is easily distinguishable. Optical micrographs of the CPG glued on to the fracture specimen, were taken before conducting the experiment to record the position of the CPG wires with respect to the ductile phase reinforcements. If the first wire was overriding the notch it was cut off with a razor blade so as not to generate a false signal of crack initiation. After the experiment, the recorded CPG voltage signal is compared with the positions of the CPG wires recorded on the optical micrographs, to estimate the crack tip velocity history.

Fig. 20 shows the microstructure ahead of the notch for a typical LDP3 fracture specimen. The dark horizontal lines represent the position of the CPG wires with respect to the position of the ductile phase reinforcements. From the optical micro-graph, it can be seen that two large and one small ductile phase reinforcements are present ahead of the initial notch tip. The LDP reinforcements in LDP3 comprise high strength Al alloy with a chemical composition very similar to the high strength 7093 Al control alloy. The corresponding load point force versus time plot is shown by the dashed line, whereas the crack propagation gage signal is shown by the solid line in Fig. 21. The time axis starts at 300 μs, which corresponds to the time of arrival of compressive pulse at the load point *E*. The total duration of the stress pulse is approximately 353 μs. The horizontal dotted lines in the figure represents the expected voltage jump as each CPG wire breaks. The experimental voltage jumps corresponding to the fracture of

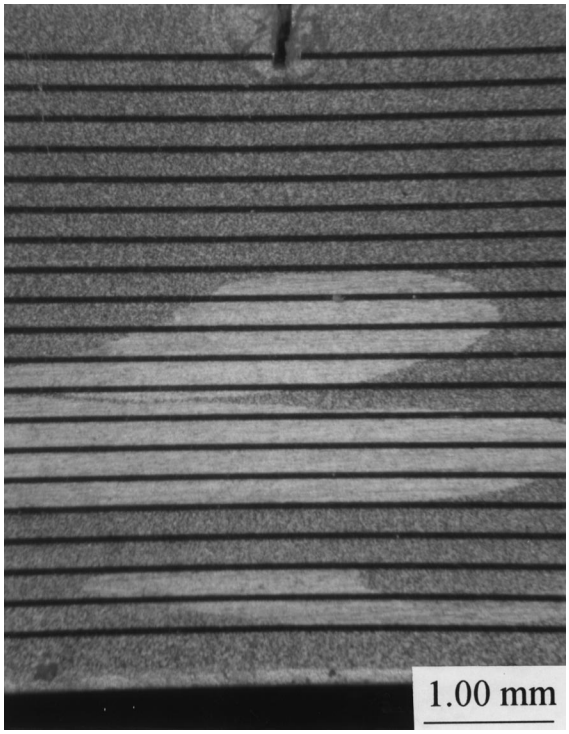

Fig. 20. Optical micrograph showing the material microstructure ahead of the pre-machined notch and the position of crack propagation gage wires with respect to the material microstructure for experiment 96-032f. The first wire overriding the notch was cut off prior to the experiment to avoid a false signal.

each CPG wires can be read from the 2*Y*-axis. Because of the relatively low band width (1 MHz) of the differential amplifier used to record the CPG output the square steps of the CPG signal are rounded off. The first peak in the load-point force versus time curve is due to inertia. The further rise in force to 5 kN represents the load-point force at crack initiation. The time for crack initiation is approximately 80 μs after the arrival of the loading pulse at the load-point end, and matches closely with the CPG signal corresponding to the fracture of the first CPG wire. Once the crack initiates the force falls sharply to 2 kN, as the increase in crack length brings down the stiffness of the specimen. As observed from Fig. 21, the first eight CPG wires lie completely in the brittle particle reinforced region. The average crack tip speed in this region, based on the time taken for the crack tip to cut through the eight CPG wires, is approximately 133.9 m/s. The crack slows down as it encounters the first bean. This is also reflected by the flat portion in the crack propagation gage signal between the 8th and the 12th wire. The average crack tip speed between the 8th and the 12th wires is 23.6 m/s. Correspondingly, the load point force in the force–time plot increases since additional energy is required to tear through the ductile phase reinforcement. Between the first and the second ductile phase reinforcement, i.e. in the brittle particle reinforced region between the 12th and the 13th wire, the crack accelerates again to a velocity of 135.8 m/s, before being slowed down as it approaches the second ductile phase reinforcement. This is again indicated by the flat region in the CPG signal between the 12th and the 13th wire. The second ductile phase reinforcement, i.e. the region between the 13th and the 16th wire, slows down the crack tip speed to 22.5 m/s. Next, the crack again accelerates to 122.5 m/s as it emerges from the second ductile phase reinforcement and enters the brittle particle reinforced region. By the time the crack reaches the last ductile phase reinforcement, i.e. the 19th wire, it has slowed down to approximately 18 m/s. The last ductile phase reinforcements lows the crack down to 2.26 m/s. The increase in load-point force corresponding to the last ductile bean is also observed in the force versus time plot. This is illustrated schematically in Fig. 22. In this figure the instantaneous speed of the crack tip is plotted as a function of position of the CPG wires on the fracture specimen. The shaded region in the figure corresponds to the position of the ductile phase reinforcement ahead of the notch tip.

Fig. 23 shows typical load-point force versus displacement curves obtained during dynamic fracture of LDP3 and LDP2 composites. The first peak in the force displacement curve occurs due to inertia; the

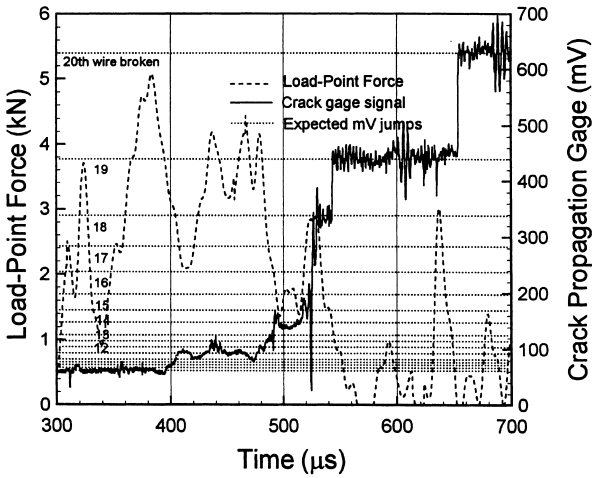

Fig. 21. Load-point force versus time profile along with the crack propagation gage (CPG) signal for experiment 96-032f. The rise and fall in the load-point force versus time profiles correlate well with the acceleration and deceleration of the crack as inferred from the crack propagation gage signal.

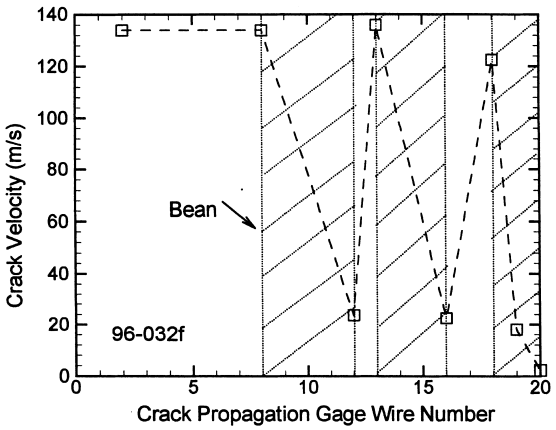

Fig. 22. Crack tip speed versus the position of the crack propagation gage wires for experiment 96-032f. The shaded region in the plot represents approximately the position of the ductile phase reinforcement. The deceleration of the crack as it interacts with the ductile phase reinforcement is clearly evident from the figure.

further rise in force, until the attainment of the highest peak represents the time before crack initiation. Once crack initiates the force falls sharply, as the extension of the crack brings down the stiffness of the specimen. As expected, the dynamic crack initiation toughness for the LDP3 composite is similar to the SDP1 and LDP2 composites. Also, the crack propagation toughness of the LDP3 composite is much higher than the SDP1 composite. The enhanced crack propagation toughness of LDP3 relative to the SDP1 composite can be attributed to extrinsic toughening mechanisms introduced by the LDP reinforcement. However, contrary to our expectations the crack propagation energy during dynamic crack propagation through the LDP3 composite is quite similar to the LDP2 composite. The crack propagation path for LDP3 composite is relatively straight as compared to the crack growth patterns observed for the LDP2 composites.

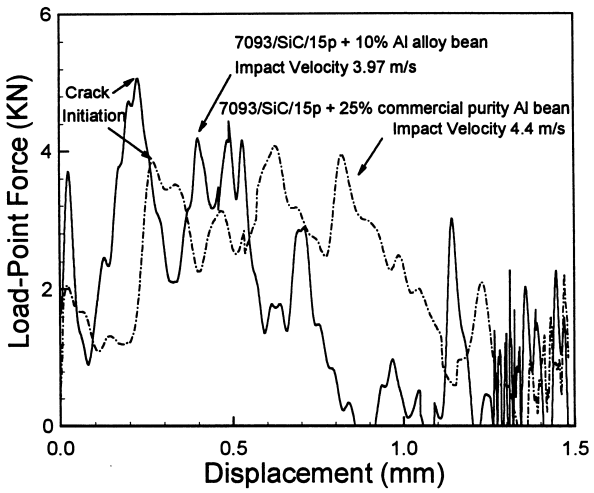

Fig. 23. Load-point force versus displacement curves for LDP2 and LDP3 composites. Both composites show similar crack initiation and propagation characteristics.

A SEM micrograph of the fracture surface with large Al alloy reinforcement is shown in Fig. 24. Unlike the large commercially pure Al reinforcement composite, the large Al alloy reinforced composite fails in a cleavage manner by inter-granular fracture. Inter-granular fracture is a low energy absorbing mechanism as compared to micro-void coalescence observed during the failure of ductile phase reinforcement in the LDP2 composites. A possible reason for the difference in the mode of failure can be attributed to the processing sequence undergone by the large Al alloy reinforced DRA composites. The large Al alloy reinforced DRA composites were extruded twice. Once in a ratio of 22:1 to produce 25.4×76.2 mm bars and then a second time to a final cross-section of 17.145×60.325 mm. As a consequence a large amount of cold work energy is stored in the composite. During the elevated temperature aging cycle, both recovery and re-crystallization processes are operative. This leads to a substantial increase in the grain size of the Al alloy phase. This is also confirmed by etching the large unreinforced ductile phase regions within the toughened DRA composites to reveal the grain boundary. The large grain size promotes cleavage failure by intra-granular fracture. Also, it is understood that overaging in Al–Zn–Mg–Cu alloys, which represents the ductile phase reinforcements in LDP3 composites, leads to grain boundary particles segregation which can result in inter-granular fracture in Al alloys (Wanhill, 1978).

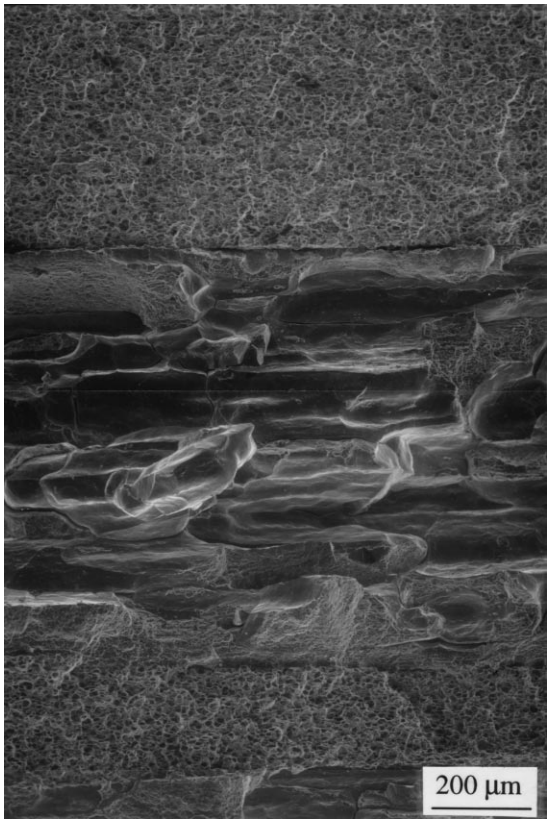

Fig. 24. Micrograph of the fracture surface for the large aluminum alloy ductile phase reinforced material (LDP3) showing inter-granular fracture. The 'brick-like' structure corresponds to a typical grain of the high strength aluminum alloy reinforcement.

5.4. Summary of dynamic fracture experiments

For all the composites evaluated in the present investigation the dynamic initiation toughness is similar to the 7093/SiC/15p composite (base material). The average energy absorbed by the composite upto crack initiation is approximately 2.25 J/cm^2. However, the dynamic crack propagation characteristics of the composites are observed to be strongly dependent on the volume fraction of the ductile phase reinforcement in the composite, the yield stress of the ductile phase reinforcement, the arrangement of the ductile phase reinforcements with respect to the notch, and the impact velocity employed in a particular experiment.

When the ductile phase reinforcement retains good ductility through processing, as in the case of the large volume fraction commercial purity aluminum reinforcements, a substantial degree of plastic stretch of the reinforcement ligaments accompanies crack growth. Notably, the ductile phase reinforcement fails in a ductile mode and ruptures along a ridge. When this occurs, without interface debonding, dynamic crack propagation shows an increase in the crack growth resistance every time the crack front encounters a ductile phase reinforcement in its path. When the ductile phase reinforcement layers are thin, as in the case of SDP1 composite, the difference in the dynamic crack growth curves for the SDP1 composite and the base composite is small. Thicker metal layers, as in the case of LDP2 and LDP3, are observed to consistently result in an increasing dynamic crack growth resistance caused by large scale bridging of the crackfront in the wake of the crack. Misalignment of the crack front and the ductile phase reinforcement layers introduces an additional level of complexity through the effects on crackpath, on crack trapping, ligament formation, etc. When the crack encounters an obliquely oriented layer, the crack is momentarily arrested and induces a series of decohesion and deformation events that dictate the subsequent behavior. At low impact velocities the LDP composites are effective as a crack arrester.

Among the LDP additions, the commercial purity aluminum consistently failed in a ductile manner with micro-void nucleation and void growth as compared to the high yield strength aluminum alloy reinforcements, which were observed to fail by a cleavage inter-granular mechanism. The combination of the various steps involved in processing the LDP3 composites, the high flow stress of the high-strength aluminum alloy reinforcement, and the constraint imposed on the deformation of the ductile reinforcement by the 7093/SiC/15p composite, are understood to be the reasons for the observed cleavage inter-granular fracture.

Acknowledgements

The research presented here was made possible in part by support from the ALCOA Technical Center, Pittsburg, PA and British Petroleum. The authors would also like to thank Prof. John Lewandowski for several enlightening discussions.

References

Ashby, M.F., Blunt, F.J., Bannister, M., 1989. Flow characteristics of highly constrained metal wires. Acta Materialia 37 (7), 1847–1857.

Bacon, C., 1993. Mesure de la tenacite dynamique de materiaux fragiles en flexion-trois-points ahaute temperature — Utilisation des barres de Hopkinson. Ph.D. Dissertation, University of Bordeaux, France.

Bacon, C., Farm, J., Lataillade, H., 1994. Dynamic fracture toughness determined from load-point displacement. Experimental Mechanics 34 (3), 217–223.

Chichili, D.R., Ramesh, K.T., 1995. Dynamic failure mechanisms in 6061-T6 Al/Al_2O_3 metal-matrix composites. International Journal of Solids and Structures 32 (17/18), 2609–2626.

Cho, K., Lee, S., Chang, Y.W., Duffy, J., 1991. Dynamic fracture behavior of SiC whisker reinforced aluminum alloys. Metallurgical Transactions A 22A, 367–375.

Christman, T., Needleman, A., Suresh, S., 1989. An experimental study of deformation in metal–ceramic composites. Acta Materialia 37 (11), 3029–3050.

Christman, T., Suresh, S., 1988. Microstructural development in an aluminum alloy SiC whisker composite. Acta Materialia 36 (7), 1691–1704.

Embury, J.D., Petch, N.J., Wraith, A.E., Wright, E.S., 1967. The fracture of mild steel laminates. Transactions of TMS-AIME 239, 114–118.

Follansbee, P.S., 1985. 9th ed., The Hopkinson Bar, Mechanical Testing, Metals Handbook, vol. 8. ASM, Metals Park, OH, pp. 198–217.

Harding, J., Taya, M., Derby, B., Pickend, S., 1987. In: Mathews, F.L (Ed.), Proceedings of the ICCM-6/ECCM-2. Elsevier, Amsterdam, pp. 2224–2233.

Hong, S.I., Gray III, G.T., 1992. Microstructure and microchemistry of an Al–Zn–Mg–Cu alloy matrix-20 vol% SiC composite. Acta Materialia 40 (12), 3299–3315.

Hong, S.I., Gray III, G.T., Lewandowski, J.J., 1993. Dynamic deformation behavior of Al–Zn–Mg–Cu alloy matrix composites reinforced with 20 vol% SiC. Acta Materialia 41 (8), 2337–2351.

Kavaturu, M., Shukla, A., 1998. Dynamic fracture criteria for crack growth along bimaterial interface. Journal of Applied Mechanics 65 (2), 293–299.

Khan, A.S., Huang, S., 1995. Continuum Theory of Plasticity. Wiley, USA.

Lambros, J., Rosakis, A.J., 1995. Dynamic decohesion of bimaterials: experimental observations and failure criteria. International Journal of Solids and Structures 32 (17/18), 2677–2702.

Lewandowski, J.J., Liu, C., Hunt, Jr., W.H., 1988. Pocessing and properties of powder metallurgy composites. In: Kumar, P., Vedula, K., Ritter, A. (Eds), The Metallurgical Society, Warrensdale PA., pp. 117–131.

Lundberg, B., Henchoz, A., 1997. Analysis of elastic waves from two-point strain measurement. Experimental Mechanics 17 (6), 213–219.

Manoharan, M., Lewandowski, J.J., Hunt Jr., W.H., 1977. Fracture characteristics of an Al–Si–Mg model composite system. Material Science and Engineering A 172 (6), 63–69.

Marchand, A., Duffy, J., Christman, T.A., Suresh, S., 1988. An experimental study of the dynamic mechanical properties of an Al–Si_w composite. Engineering Fracture Mechanics 30, 295–315.

Nakamura, T., Shih, C.F., Freund, L.B., 1986. Analysis of a dynamically loaded three-point bend ductile fracture specimen. Engineering Fracture Mechanics 25, 323–339.

Nardone, V.C., Strife, J.R., Prewo, K.M., 1991. Microstructurally toughened particulate reinforced aluminum matrix composites. Metallurgical Transactions A 22A, 171–182.

Nemat-Nasser, S., Issacs, J.B., Starrett, J.E., 1991. Hopkinson bar techniques for dynamic recovery experiments. Proceedings of Royal Society of London A435, 371–391.

Osman, T.M., Lewandowski, J.J., Hunt Jr., W.H., Lesuer, D.R., Riddle, R., 1995. Extrinsic toughening in DRA laminates. In: Lewandowski, J.J., Hunt Jr., W.H. (Eds.), Intrinsic and Extrinsic Fracture Mechanisms in Inorganic Systems. The Minerals, Metals and Materials Society, Warrendale, PA, pp. 103–112.

Perng, C.C., Hwang, J.R., Doong, J.L., 1993. The effects of strain-rate on the tensile properties of an Al_2O_3/6061T6 aluminum metal matrix composites at low temperatures. Scripta Materialia 29, 311–316.

Plati, E., Williams, J.G., 1975. The determination of the fracture parameters for polymers in impact. Polymer Engineering and Science 15 (6), 470–477.

Ramesh, K.T., Coates, R.S., 1992. Microstructural influences on the dynamic response of tungsten heavy alloys. Metallurgical Transactions A 23A, 2625–2630.

Shaw, M.C., Clyne, T.W., Cocks, A.C., Fleck, F., Pateras, N.A., 1996. Cracking patterns in metal-ceramic laminates: effects of plasticity. Journal of the Mechanics and Physics of Solids 44, 801–821.

Sherby, O.D., Lee, S., Koch, R., Sumi, T., Wolfenstine, J., 1990. Multilayered composites based on ultrahigh carbon steel and brass. Materials and Manufacturing Processes 5, 363–376.

Siegmund, T., Fleck, N.A., Needleman, A., 1997. Dynamic crack growth across an interface. International Journal of Fracture 85, 381–407.

Singh, R.P., Shukla, A., 1996. Subsonic and transonic crack growth along a bimaterial interface. Journal of Applied Mechanics 63, 919–924.

Syn, C.K., Lesuer, D.R., Cadwell, K.L., Sherby, O.D., Brown, K.R., 1991. Laminated metal composites of ultrahigh carbon steel/brass and Al/Al-SiC: processing and properties. In: Upsadhya, K. (Ed.), Developments in Ceramic and Metal Matrix Composites. TMS, Warrendale, PA, pp. 311–323.

Walkup, J.R., 1994. Influence of volume fraction reinforcement on the mechanical properties of a magnesium/SiC_p metal matrix composite. M.S. Thesis, Case Western Reserve University, Cleveland, OH.

Wanhill, R.J.H., 1978. Microstructural influences on fatigue and fracture resistance in high strength structural materials. Engineering Fracture Mechanics 10, 337–357.

Yadav, S., Chichili, D.R., Ramesh, K.T., 1995. The mechanical response of a 6061-T6Al/Al_2O_3 metal matrix composite at high rates of deformation. Acta Materialia 43 (12), 4453–4464.